Engineering secretory amyloids for remote and highly selective destruction of metastatic foci

María Virtudes Céspedes, Olivia Cano-Garrido, Patricia Álamo, Rita Sala, Alberto Gallardo, Naroa Serna, Aïda Falgàs, Eric Voltà-Durán, Isolda Casanova, Alejandro Sánchez-Chardi, Hèctor López-Laguna*, Laura Sánchez-García, Julieta M. Sánchez, Ugutz Unzueta, Esther Vázquez*, Ramón Mangues*, Antonio Villaverde**

Dr. María Virtudes Céspedes, Dr Patricia Álamo, Rita Sala, Dr Alberto Gallardo, Aïda Falgás, Dr. Isolda Casanova, Dr Ugutz Unzueta, Prof Ramón Mangues
CIBER de Bioingeniería, Biomateriales y Nanomedicina (CIBER-BBN), C/ Monforte de Lemos 3-5, 28029 Madrid, Spain
Institut d'Investigacions Biomèdiques Sant Pau and Josep Carreras Research Institute, Hospital de la Santa Creu i Sant Pau, 08041 Barcelona, Spain
Dr Olivia Cano-Garrido, Dr Naroa Serna, Dr Laura Sánchez-García, Eric Voltà, Hèctor López-Laguna, Dr Julieta M. Sánchez, Dr Esther Vázquez, Prof Antonio Villaverde
Institut de Biotecnologia i de Biomedicina, Universitat Autònoma de Barcelona, Bellaterra, 08193 Barcelona, Spain
Departament de Genètica i de Microbiologia, Universitat Autònoma de Barcelona, Bellaterra, 08193 Barcelona, Spain
CIBER de Bioingeniería, Biomateriales y Nanomedicina (CIBER-BBN), C/ Monforte de Lemos 3-5, 28029 Madrid, Spain
Dr Olivia Cano-Garrido
Nanoligent SL, Edifici EUREKA, Universitat Autònoma de Barcelona, Bellaterra, 08193 Barcelona, Spain
Dr Alejandro Sánchez-Chardi
Servei de Microscòpia, Universitat Autònoma de Barcelona, Bellaterra, 08193 Barcelona, Spain
Dr Julieta M. Sánchez
Instituto de Investigaciones Biológicas y Tecnológicas (IIBYT) (CONICET-Universidad Nacional de Córdoba). ICTA & Cátedra de Química Biológica, Departamento de Química, FCEFyN, UNC. Av. Velez Sarsfield 1611, X 5016GCA Córdoba, Argentina
* Corresponding authors

Keywords: protein materials, secretory amyloids, self-assembling, drug release, metastatic cancer

Esther Vazquez *Esther.Vazquez@uab.es*
Ramón Mangues *rmangues@santpau.cat*
Antonio Villaverde *antoni.villaverde@uab.cat*

Functional amyloids produced in bacteria as nanoscale inclusion bodies are intriguing but poorly explored protein materials with wide therapeutic potential. Since under physiological conditions they release functional polypeptides, these materials could be potentially tailored as mimetic of secretory granules for slow systemic delivery of smart protein drugs. To explore this possibility, bacterial inclusion bodies formed by a self-assembled, tumor-targeted *Pseudomonas* exotoxin (PE24) have been administered subcutaneously in mouse models of human metastatic colorectal cancer, for sustained secretion of tumor-targeted therapeutic nanoparticles. These proteins are functionalized with a peptidic ligand of CXCR4, a chemokine receptor overexpressed in metastatic cancer stem cells that confers high selective cytotoxicity *in vitro* and *in vivo*. In mouse models of human colorectal cancer, time-deferred anticancer activity is detected after the subcutaneous deposition of 500 μg of PE24-based amyloids, which promotes a dramatic arrest of tumor growth in absence of side toxicity. In addition, long-term prevention of lymphatic, hematogenous and peritoneal metastases is achieved. These results reveal the biomedical potential and versatility of bacterial inclusion bodies as novel tunable secretory materials usable in delivery, and they also instruct how therapeutic proteins, even with high functional and structural complexity, can be packaged in this convenient format.

Bacterial inclusion bodies (IBs) are naturally occurring protein clusters commonly observed in recombinant bacteria. [1] Being the transgene protein product their main component, they are mechanically stable, soft proteinaceous particles [2] in between nano and micro scales (usually ranging from 50 to 1500 nm in size). A fraction (about 40 %) of the recombinant protein is organized as non-toxic amyloid fibers and the remaining protein component is found in a proteinase-K sensitive, functional or quasi-functional form. [3] Since the discovery of the biological activity associated to IB protein, [4] IBs have been exploited as self-immobilized catalysts for chemical and biotechnology industries [5] and also as protein carriers for intracellular delivery of functional proteins, in form of nanopills. [6] This is because IBs tend to interact with mammalian cell membranes in absence of toxicity and penetrate exposed cells where the embedded protein is functional in both IB-associated and upon eventual release from IBs. In materials sciences, IBs have been explored as functional topographies in tissue engineering, [7] to simultaneously provide mechanical and biological stimuli to growing cells. [8] More recently, it has been demonstrated that bacterial IBs can be targeted to specific cell types, either by chemical [6a] or biological [9] engineering approaches. In addition to this, IBs formed by cell-targeted polypeptides (for instance containing a tumor-homing amino acid stretch) can release *in vivo* soluble protein from IB [10] that reaches target organs through the blood stream. [11] The delivery of IB protein *in vivo* appears to be a physiological (secretion-like) rather than a diffusional chemical process, [10, 12] in which biological factors such as chaperones seem to be involved. Such findings have enormous biomedical relevance, as IBs might be adapted, as novel smart materials, as an *in vivo* source of protein drugs for precision therapy mimicking the activity of the amyloidal protein granules of the human endocrine system. [13] To evaluate the use of bacterial IBs as artificial secretory granules adapted to clinical applications, we have designed and generated IBs formed by the modular polypeptide T22-PE24-H6 (**Figure 1A and Figure S1**). In the amino terminus, this protein displays the peptide T22, a powerful CXCR4 ligand that allows specific $CXCR4^+$ cell binding and

internalization. [14] In previous studies, T22 has been shown as promising to selectively internalyze macromolecular complexes into CXCR4-overexpressing cells and therefore useful to deliver conventional antitumoral drugs (e.g. fluoroxyuridine) to tumor tissues for the targeted destruction of $CXCR4^+$ metastatic foci. [15] PE24 is a domain of the *Pseudomonas aeruginosa* exotoxin, a promising cytotoxic protein drug under clinical trials for cancer treatment, mainly in form of immunotoxins. [16] The carboxy terminal H6 is a polyhistidine tail that promotes the self-assembling of the building blocks via divalent cation coordination as CXCR4-targeted protein nanoparticles of around 50 nm in size. [17] Under repeated intravenous administration, these nanoparticles effectively and selectively destroy primary tumor tissues in mice models of human colorectal cancer. [17] In this context, we wondered if T22-PE24-H6, already confirmed as effective antitumoral drug, could be produced as functional, protein-releasing IBs for further testing as therapeutic agents in animal cancer models after subcutaneous deposition. A sustained release of the protein from implanted repositories should prevent high peak levels associated with conventional intravenous injection of punctual doses. We also wondered whether the released material, if any, would be organized as nanostructured protein oligomers as it occurs with the soluble version of T22-PE24-H6 as straightforward recovered from producing bacterial cells.

The recombinant protein was produced in *Escherichia coli* Origami B, encoded by a pET22b-derivative (Figure S1), and whose synthesis was induced by 1 mM IPTG at 37 ºC for 3 h. An excellent yield of 70 mg/L cell culture was straightforward observed, what appears as promising regarding potential scaling-up or further optimization, if large-scale production should be considered in a future. More than 50 % of the protein was found as insoluble material (Figure 1B), in form of conventional, pseudoespherical IBs of about 200 nm (precisely 207.0 ± 4.9 nm, Figure 1C). When exposed to cultured $CXCR4^+$ HeLa cells, these materials resulted toxic (Figure 1G) due to the presence of the PE24 segment. However, IBs formed by the closely related T22-GFP-H6 (Figure 1A), used here as non-functional control

(the GFP fluorescence, still observable in IBs, does not provoke any known biological response) were irrelevant regarding cell viability (Figure S2). Cell death was mediated by specific T22-CXCR4 interactions, since the CXCR4 antagonist AMD3100 [18] prevented cell killing when added to the cultures prior to IB exposure (Figure 1H). Upon purification, PE24-based IBs were incubated *in vitro* in physiological buffer for a few days.

Under this experimental setting, we detected a progressive increase of soluble T22-PE24-H6 in the supernatant of the suspension (Figure 1D, E) that organized as nanostructured materials (Figure 1F). Note that smaller entities, namely monomeric building blocks, were not observed in any sampling time, indicating structural and proteolytic robustness of the material. These nanoparticles, already detected in the shortest analyzed time (3 h), were morphologically indistinguishable from those obtained from straightforward purification of soluble protein from producing bacteria (Figure S3),[17, 19] although their size was slightly smaller at prolonged incubation times. These data were indicative of progressive protein release from IBs not linked to any proteolytic event. Such release process, if sufficiently efficient and time-sustained, might have a clinical value.

In this context, and to explore in detail the potential systemic use of IBs as a novel drug-releasing material, we administered T22-PE24-H6 IBs to metastatic mouse models derived from human colorectal and based on$CXCR4^+$ SW1417-luciferase expressing cells. [15] Note that as previous reference, we had determined the biodistribution of a fluorescent protein material released from IBs formed by T22-empowered GFP, which followed the expected biodistribution and tumor accumulation. [11] Because of such promising data, two different doses of the protein material developed here were subcutaneously (SC) injected in the anterior flank of mice (**Figure 2A**), to evaluate the dose-dependence of any potential therapeutic effect. The objective of this administration route was to explore the long-term healing effects of the material released from the IB reservoirs, in contrast with the short administration

intervals between repeated doses applied during the intravenous administration of CXCR4-targeted toxins.

A two-dose administration of PE24 IBs (Figure 2A) resulted in a dramatic arrest of primary tumor cell growth, which was absolute under 500 μg and milder when immobilizing 200 μg IB per dose in the subcutis of the animals (Figure 2B). Growth inhibition of both primary tumor and metastatic foci at different organs was determined by reduction of bioluminescence emission by SW1417-luciferase expressing cancer cells (Figure 2B, C). The antitumoral effect reached in primary tumor was accompanied by a dramatic reduction in metastatic foci during treatment time (**Table 1**). As observed, at the end of the assay, hepatic metastases completely disappeared in all treated animals, irrespective of the given dose, a fact that reflects a powerful antimetastatic potential of T22-PE24-H6, apart from the known effect on primary tumor, never observed before. [17] A dose-independent reduction in the number of animals in which metastases were detected was also achieved in other tested tissues (Table 1). The obtained data indicated that at a dose of 200 μg, the antimetastatic effect of PE24 probably reached a plateau, while the antitumoral effect on primary tumor was still in a dose-dependent phase. Mouse necropsies, performed at the end of the experiment, 29 days upon tumor cell implantation, followed by histological evaluation of the primary tumor, revealed a dramatic increase of apoptotic cells, responsible for the antitumoral and antimetastatic effects, which were more intense at the 500 μg dose (Figure 2E). This result was associated with a local reduction in the number of $CXCR4^+$ cells in tumor (Figure 2F), the target of T22-PE24-H6. All these therapeutic events, including the desired and newly described reduction of metastatic foci, occurred in absence of detectable changes in the body weight of treated mice (**Figure 3A**), indicative of a lack of acute systemic toxicity promoted by either the source protein material and the released nanoparticles. The absence of side effects was confirmed by the lack of histopathological alterations, and by the non-relevant morphological changes in major organs such as lung, liver and kidney (Figure 3B). At the injection site (Figure 3C), no

edema, material deposition or massive inflammatory cell infiltration were observed, except for a slight lymphocyte infiltration at the end of the experiment at the highest used dose (500 μg). On the other hand, no proteolytic degradation of T22-PE24-H6 was observed during 10 days of incubation with human sera under physiological conditions (Figure 3 D). Since no monomers were detectable during such incubation (Figure 3E), a robust oligomeric architecture and proteolytic stability of T22-PE24-H6 nanoparticles, that did not disassemble, was fully confirmed.

To discard that the observed antitumor effects might be linked to protein domains or IB agents other than PE24, we tested any potentially residual cytotoxic activity associated to control T22-GFP-H6 IBs, formed by the protein construct in which GFP is placed instead PE24. Data in Table S1 show the absence of detectable biological effects of this material on primary tumor and on organs affected by metastasis. In addition, a biodistribution study of the IB-released T22-GFP-H6 nanoparticles was performed by measuring the emitted green fluorescence (FLI) and GFP protein amounts by Western blot (WB) along time (namely 10 min, and 2, 5, 10 or 15 days after 1 mg IB injection). As expected, we observed a kinetic reduction of the amount of protein by WB and of emitted total fluorescence at the IB injection site (Figure S4 A) in parallel to a sustained increase of total FLI in the remote tumor tissue (Figure S4 B), without accumulation in liver or kidney at any tested time (not shown). However, we were unable to determine the nanoparticle PK by in blood either by WB or by FLI emission (because of the high fluorescence background). In contrast, in a prior report, and after a single 200 μg intravenous bolus injection of soluble T22-GFP-H6 nanoparticles in the same mouse model, we detected full-length protein by WB using an anti-GFP mAb, at 10 min, in liver and kidney. In there, most likely, the nanoparticles transiently accessed the fenestrated vessels, returning to blood without being uptaken. Full-length protein was also observed at the injection site within the 2-15 day range (Figure S4 C), but not in tumor and in any other tested tissue (not shown). These data might indicate a low sensitivity for FLI or WB

for the detection of soluble nanoparticle released from the IBs (its sustained release might maintain nanoparticle concentration low in blood, despite of being extended in time). This possibility is fully supported by the easy detection within the 0-48 h period, using the same FLI and WB techniques, of the full-length protein in blood, and full-length and proteolyzed protein in tumor tissue (but not in liver or kidney, except at 10 min). [20]

Taken together, all these observations, including those involving the control T22-GFP-H6 material *in vitro* and *in vivo*, supported the specificity of the treatment and the successful targeting of a highly cytotoxic protein, in form of protein-only nanoparticles, from a remote implantation site. The data also validated T22-PE24-H6 as a structurally robust anti-metastatic agent that in an oligomeric form, performed in an excellent way, in form of stable CXCR4-targeted nanoparticles and in absence of proteolytic degradation and toxin leakage during the circulation and permanence in the blood stream.

Several types of materials are under exploration as drugs repositories for slow release, including hydrogels [21] and a diversity of structured mesoporous composites. [22] These materials are loaded with relevant drugs that result mechanically entrapped in the network and further released by dilution into the surrounding media. Although they have shown promise in cancer treatments, the recalcitrant nature of some of the used scaffolds or matrices, such as metals, [23] pose reasonable concerns about their safety after long-term use in complex biological systems such as entire organisms. Bacterial IBs composed by the protein drug itself as building block, represent a fully biocompatible, protein-only material. Being chemically homogeneous, it is progressively disintegrated under physiological conditions or *in vivo* into smaller protein components (here 50 nm-nanoparticles) , probably with the intervention of chaperones or other factors present in the extracellular media or in the material itself[10, 12] but irrespective of any significant proteolytic event. This appears to be the mechanistic functioning of secretory granules in the human endocrine system, [13a] in which protein hormones are released from amyloid-based protein clusters that bacterial IBs effectively

mimic. Upon a harsh IB purification protocol from producing bacteria [24] the remaining amounts of bacterial cell contaminants are probably kept at sub-toxic levels, since no side toxicity in treated animals was observed after a few weeks of treatment (Figure 3). The occurrence of bacterial endotoxins in IBs derived from conventional K-12 *E. coli* strains has been roughly estimated to be lower than 0.1 mg of lipopolysaccharide per mg of IB protein (not shown). Being insufficient to generate inflammation at the injection site (Figure 3 C), this is still an issue to be considered during further IB development. However, since functional IBs or IB-like particles have been successfully produced in endotoxin-free strains of *E. coli*, [25] in food-grade lactic acid bacteria [26] and also in yeasts, [27] the future clinically-oriented development of secretory amyloids must necessarily consider these safer cell factories, favourable for the production of protein-based drugs [28] from strategic and regulatory point of views. Considering that any IB-forming polypeptide with therapeutic value can also be engineered to acquire specific cell targeting, as in the case of T22-PE24-H6, the implantable material can be designed for precision medicines such as in cancer treatments. In that case, the IB-based platform promotes secretion rather than drug release, acting as a mimetic of the endocrine system instead of a conventional drug-release agent. Here, such novel IB-based platform shows a predictable sustained release kinetics, which could mainly depend on the factor-mediated dissociation constant that generates soluble protein from the aggregated IB form. Moreover, the model IBs presented here release soluble nanoparticles that achieve a highly selective biodistribution in target tissues. This is in sharp contrast with the conventional drug-release agents, which achieve a highly variable drug levels in target tissue because of their difficulty in controlling drug release (depending on their excipient formulation, interactions with the injection site and degradation during release) and the lack of selectivity of the released therapeutic agents. [29] Both aspects are conceptually solved by the secretion of soluble, self-assembled nanoparticles from IBs engineered for that purpose. Besides this, the abundance of cytotoxic proteins (toxins and venom components) in use or

under development for cancer treatments [30] makes bacterial IBs promising particulate biomaterials for the development of specific antitumoral products, based on these protein toxins or their combinations. The potent antimetastatic properties of the *Pseudomonas* exotoxin PE24 firstly shown here as released from IBs in a CXCR4-targeted form (Figure 2, Table 1), and the systemic release of the drug from the implantation site, make the proposed IB-based platform especially appealing for the treatment of disseminating forms of cancer under fully physiological and biosafe conditions.

Experimental section

Protein design, production, purification and biophysical characterization

Genes encoding T22-PE24-H6 and T22-GFP-H6 were harbored in *Escherichia coli* Origami B (BL21, OmpT$^-$, Lon$^-$, TrxB$^-$, Gor$^-$, Novagen). GFP in T22-GFP-H6 was used as a control of a core peptidic element in the modular protein lacking any relevant biological activity. Both proteins were produced as IBs for 3 h at 37 °C upon addition of 1 mM isopropyl-β-d-thiogalactopyranoside (IPTG). IBs were purified by a protocol for proteins with high tendency to become soluble. [24] The amount of protein was quantified by WB using anti-His monoclonal antibody (Genscript). The amount of recombinant protein was estimated by comparison with a GFP-H6 calibration curve. Far-UV circular dichroism (CD) was measured at 25 ºC in a Jasco J-715 spectropolarimeter to collect secondary structure information. Protein concentration was adjusted to 0.2 mg/mL in a buffer solution of 166 mM carbonate-bicarbonate at pH 8. CD spectra were obtained with a 1 mm pathlength cuvette over a wavelength range of 200-240 nm at a scan rate of 100 nm/min. A response of 2 s and a bandwith of 1 nm 13 scans were accumulated. The spectra were processed through a negative exponential with a sampling proportion of 0.1 and 1 polynomial degree.

Ultrastructural characterization

To study the morphometry of IBs (size and shape), insoluble protein was resuspended in phosphate buffered saline (PBS) at 10 mg/ml and sonicated at 10 % amplitude 0.5 s ON/OFF for 1 min. High resolution imaging at a nearly native state of protein aggregate suspension at 0.25 mg/ml was performed with four electron microscopy techniques. For field emission scanning electron microscopy (FESEM), microdrops of samples were deposited during 2 min on silicon wafers (Ted Pella Inc.), air-dried and observed in a FESEM Merlin (Zeiss) operating at 2 kV and equipped with a conventional secondary electron (SE) detector. For conventional TEM, microdrops of sample were deposited in two carbon-coated copper grids

(300 mesh) during 1 min. One of the grids was air-dried and other was incubated 2 min with 2% uranyl acetate and air-dried. Both direct deposited and negative stained grids were observed with a TEM JEM-1400 (Jeol) operating at 80 kV and equipped with a Orius SC 200 CCD camera (Gatan Inc.). Finally, for cryo-TEM, a microdrop of sample was deposited in a Holey carbon-coated copper grid (400 mesh), cryofixed in liquid ethane with an EM GP automatic plunge freezer (Leica), placed in a cryo-transfer specimen holder (Gatan Inc.) and observed in a TEM JEM-2011 (Jeol) operating at 200 kV and equipped with a 895 USC 4000 CCD camera (Gatan Inc.). To study the morphometry of nanoparticles, microdrops of samples at 0, 3, 24 and 48 h at 10 mg/ml were deposited during 2 min on silicon wafers (Ted Pella Inc.), air-dried and observed in a FESEM Merlin (Zeiss), operating at 1 kV and equipped with a high resolution *in-lens* secondary electron (SE) detector. A quantitative analysis of particle size was performed with a total number of 80 T22-PE24-H6 IB and 423 T22-PE24-H6 nanoparticles using Image J software.

Protein release in vitro

T22-PE24-H6 purified IBs were resuspended in PBS at 10 mg/ml and incubated at 37 °C. Samples were taken at 0, 3, 24, and 48 h and centrifuged for 15 min at 15,000 *g* and 4 °C. Soluble and insoluble fractions were further processed for WB and FESEM imaging. In all the cases, pellets corresponding to the insoluble fraction (IBs) were resuspended in PBS at the same final volume than their soluble counterpart for comparison.

Functional characterization in vitro

HeLa cells (ATCC-CCL-2) were cultured at 37 ºC in a 5 % CO_2 humidified atmosphere in MEM-Alpha media supplemented with 10 % fetal calf serum (Gibco). They were seeded in an opaque 96-well plate (3500 cells/well) for 24 h, the media was supplemented with 2 % penicillin and streptomycin Sol 10,000 U/ml (Gibco). Next, different concentrations of T22-

PE24-H6 IBs (namely 10, 100, 1000, 5000 and 10000 nM) and 10000 nM of T22-GFP-H6 IBs as a control were incubated at 48 h. In addition, in some wells insoluble protein was incubated without HeLa cells as a control. The extent of living cells was determined by adding of CellTiterGlo Luminescent Cell Viability Assay (Promega) and reading in a Multilabel Plater Reader Victor3 (Perkin Elmer). For the CXCR4 specificity assay, the CXCR4 antagonist AMD3100 [18a, 18c, 31] was added at 1:10 molar ratio 1 hour before the incorporation of the protein. Antagonist and protein were incubated in a final volume of 10 µl. All soluble protein experiments were done in with six replicates. To calculate the T22-PE24-H6 IC50 dose, data was fit to a cubit equation, which has been solve by using the Vieta formula.

Stability in human serum

Soluble T22-PE24-H6 nanoparticles (at 1 mg/mL) were incubated with 2 mg/mL of Human Serum (Sigma-Aldrich) at 37ºC without agitation for different incubation times (0 h, 1 h, 4 h, 48 h, 5 d and 10 d) in final volume of 100 µL. All the experimental processes were performed in sterile conditions and buffers and solutions were filtered in 0.22 µm. Then, protein integrity was measured in Tris-Glycine eXtended Stain-Free Gels (TGX) and by WB (1:5000 Anti-His Santa Cruz Biotechnology, ref: sc-57598). The oligomeric structure was determined by Dynamic Light Scattering (DLS).

Evaluation of T22-GFP-H6 biodistribution and pharmacokinetics

We used Swiss nude mice (Charles River, L-Abreslle, France) to generate a subcutaneous (SC) mouse model by implanting 10 mg of $CXCR4^+$ SW1417 tumor tissue from donor animals in the mouse flank. When tumors reached approximately 150 mm^3, mice (n=3) were subcutaneously administered in the back of the mice (located remote form the tumor) with a

single 1,000 μg dose of T22-GFP-H6 bacterial IBs resuspended in a 250 μl saline solution. Control mice were administered with the same volume of saline solution. We sacrificed three mice per each time point, at 10 minutes and 2, 5, 10 and 15 days after the administration and took the tissue that included the injection point, the tumor, the normal liver and kidney to measure *ex vivo* their emitted fluorescence using the IVIS® Spectrum (Perkin Elmer, USA) platform. The fluorescent signal (FLI), was first digitalized, displayed as a pseudocolor overlay, and expressed as total radiant efficiency [(p/sec/cm2/sr)/μW/cm2]. We also obtained approximately 0.5 ml of blood in EDTA-anticoagulated tubes, to measure the exact volume of plasma and the emitted fluorescence at each time point. In addition, we cryopreserved samples in liquid nitrogen for protein extraction and to measure the amount of T22-GFP-H6 protein by WB at the injection point, tumor, liver and kidney as previously described. [20]

Evaluation of antitumoral and antimetastatic activity

To evaluate the effect of IBs material we used human tumor xenograft models. These in vivo models have a high degree of correlation between sensitivity of disease-specific human xenografts and complete clinical response rates implantation. [32] In addition, the orthotopic implantation, which involves injecting cancer lines into the physiologic site corresponding to the cancer tissue type are more likely to produce tumor metastases due to the microenvironment and the well-defined vessel system of organ. [33] In this context, five-week-old female Swiss nu/nu mice weighing between 18 and 20 g (Charles River, L-Abreslle, France) and maintained in SPF conditions, were used for the *in vivo* experiment. *In vivo* procedures were approved by the Hospital de Sant Pau Animal Ethics Committee and performed according to European Council directives. To generate metastatic CCR cancer mouse model, Swiss nude mice were anesthetized with a mixture of ketamine (100 mg/kg) and xylazine (10 mg/kg), exteriorizing their cecum by a laparotomy. 2×10^6 $CXCR4^+$ SW1417 CRC cells (expressing luciferase, to allow *ex vivo* bioluminescent identification of

metastatic foci in affected organs) were suspended in 50 µl of modified Eagle's medium and loaded into a sterile micropipette as described elsewhere. [34] A week before the orthotopic implantation, mice were randomly allocated and administered subcutaneously (by deposition), in the anterior flank with bacterial T22-PE24-H6 IBs at 200 or 500 µg/dose resuspended in a 150 µl saline solution (n=5/group/dose) or the control mice (n=5) administered with the same volume of saline solution. A dose was given each 10 days and two doses total according to previously reported.[11] After IB administration, mouse body weights were recorded and whole-body mice were monitored by bioluminescent image (BLI) twice a week to determine tumor progression using the IVIS® Spectrum equipment (PerkinElmer Inc.). At necropsy, BLI was recorded *ex vivo* in primary tumor, mesenteric, liver, diaphragm, lung and kidney organs using the IVIS equipment and then, samples were formalin-fixed and paraffin-embedded for histology and immunohistochemistry analyses. A control anticancer efficacy experiment was performed using the $CXCR4^+$ SW1417 colorectal cancer orthotopic model and following the same procedure described above, to assess whether the SC administration of T22-GFP-H6 bacterial IBs (experimental group, n=6) displayed antitumor or antimetastatic activity as compared to vehicle-injected mice (n=6). Mice received a first dose of 500 µg (n=6/group) followed by an equal second dose 10 days after. Twelve days after the second dose, mice were euthanized and samples of primary tumor, mesenteric, liver, lung and peritoneal membrane were collected to perform histopathological analyses, counting the number of metastases per organ and their size.

Histopathology and immunohistochemistry analyses

Four-micrometer-thick sections were stained with hematoxylin and eosin (H&E), and a complete histopathological analysis was performed in the target organs and the point of injection by two independent observers. The number of apoptotic figures in tumors was quantified by counting the number of positive cells per 10 high-power fields (magnification

400x). The expression of the CXCR4 was assessed by immunohistochemistry using the DAKO immunosystem equipment and standard protocols. A primary antibody against CXCR4 (1:300; Abcam) was incubated for 25 min to detect CXCR4 presence in tumor tissues. The percentage of CXCR4-expressing cells in relation to the total cell number in each primary tumor section (N=5/group) were recorded at 400x magnification. Representative images were taken using Cell^B software (Olympus Soft Imaging v 3.3).

Statistical analyses

Pairwise comparisons of protein cytotoxicity effect were made with Mann-Whitney U-tests and competition assay with Student t-test. Fisher's exact test to detect differences between control and experimental groups of affected mice regarding metastatic rates and sizes at the different organs. Finally, multiple comparison with Kruskal-Wallis and Mann-Whitney U-tests were used to compare tumor tissue BLI, the number and size of metastatic foci in the affected organs, the number of apoptotic bodies, and the percentage of CXCR4-expressing cells. All statistical tests were performed using SPSS version 11.0. All quantitative values both *in vitro* and *in vivo* experiments were expressed as mean ± standard error ($\overline{x}$ ± SD). Differences among groups were considered significant at $p < 0.05$.

Acknowledgements

VC, OCG and PA have equally contributed to this study. We thank Carmen Cabrera for her technical support in the Nanotoxicology Unit Platform. We are indebted to Agencia Estatal de Investigación (AEI) and to Fondo Europeo de Desarrollo Regional (FEDER) (grant BIO2016-76063-R, AEI/FEDER, UE) to AV, AGAUR (2017SGR-229) to AV and 2017SGR-865 GRC to RM; CIBER-BBN (project NANOPROTHER) granted to AV, CIBER-BBN project 4NanoMets to RM and CIBER-BBN project NANOREMOTE to EV; ISCIII (PI15/00272 co-founding FEDER) to EV and ISCIII (Co-founding FEDER) PIE15/00028 and PI18/00650 to

RM, and to EU COST Action CA 17140. We are also indebted to the Networking Research Center on Bioengineering, Biomaterials and Nanomedicine (CIBER-BBN) that is an initiative funded by the VI National R&D&I Plan 2008–2011, Iniciativa Ingenio 2010, Consolider Program, CIBER Actions and financed by the Instituto de Salud Carlos III, with assistance from the European Regional Development Fund. Protein production has been partially performed by the ICTS "NANBIOSIS", more specifically by the Protein Production Platform of CIBER in Bioengineering, Biomaterials & Nanomedicine (CIBER-BBN)/ IBB, at the UAB sePBioEs scientific-technical service (http://www.nanbiosis.es/portfolio/u1-protein-production-platform-ppp/) and the *in vitro* assays at the Cell Culture Unit (SCAC at UAB). Biodistribution studies were performed by the ICTS "NANBIOSIS", Nantoxicology Unit (http://www.nanbiosis.es/portfolio/u18-nanotoxicology-unit/). All *in vivo* experiments were performed by the ICTS "NANBIOSIS", more specifically by the CIBER-BBN's *In Vivo* Experimental Platform at the Nanotoxicology Unit (http://www.nanbiosis.es/unit/u20-in-vivo-experimental-platform/). Electron microscopy studies were performed by the Servei de Microscòpia at the UAB. AV received an ICREA ACADEMIA award. MVC was supported by a Miguel Servet contract and from ISCIII, and RS by the ISCIII PFIS fellowship FI16/00017. LSG was supported by a predoctoral fellowship from AGAUR (2018FI_B2_00051), HLL by a predoctoral fellowship from AGAUR (2019FI_B_00352), EVD by a predoctoral fellowship by Ministerio de Ciencia, Innovación y Universidades (FPU18/04615) and UU by PERIS program from the Health Department of la Generalitat de Catalunya.

Received: ((will be filled in by the editorial staff))
Revised: ((will be filled in by the editorial staff))
Published online: ((will be filled in by the editorial staff))

References

1. de Marco, A.; Ferrer-Miralles, N.; Garcia-Fruitos, E.; Mitraki, A.; Peternel, S.; Rinas, U.; Trujillo-Roldan, M. A.; Valdez-Cruz, N. A.; Vazquez, E.; Villaverde, A., Bacterial inclusion bodies are industrially exploitable amyloids. *FEMS microbiology reviews* **2019,** *43* (1), 53-72.

2. Rinas, U.; Garcia-Fruitos, E.; Corchero, J. L.; Vazquez, E.; Seras-Franzoso, J.; Villaverde, A., Bacterial Inclusion Bodies: Discovering Their Better Half. *Trends in biochemical sciences* **2017,** *42* (9), 726-737.

3. Cano-Garrido, O.; Rodriguez-Carmona, E.; Diez-Gil, C.; Vazquez, E.; Elizondo, E.; Cubarsi, R.; Seras-Franzoso, J.; Corchero, J. L.; Rinas, U.; Ratera, I.; Ventosa, N.; Veciana, J.; Villaverde, A.; Garcia-Fruitos, E., Supramolecular organization of protein-releasing functional amyloids solved in bacterial inclusion bodies. *Acta biomaterialia* **2013,** *9* (4), 6134-42.

4. Gonzalez-Montalban, N.; Garcia-Fruitos, E.; Villaverde, A., Recombinant protein solubility - does more mean better? *Nature biotechnology* **2007,** *25* (7), 718-20.

5. (a) Hrabarova, E.; Achbergerova, L.; Nahalka, J., Insoluble protein applications: the use of bacterial inclusion bodies as biocatalysts. *Methods in molecular biology* **2015,** *1258*, 411-22; (b) Krauss, U.; Jager, V. D.; Diener, M.; Pohl, M.; Jaeger, K. E., Catalytically-active inclusion bodies-Carrier-free protein immobilizates for application in biotechnology and biomedicine. *Journal of biotechnology* **2017,** *258*, 136-147; (c) Jager, V. D.; Kloss, R.; Grunberger, A.; Seide, S.; Hahn, D.; Karmainski, T.; Piqueray, M.; Embruch, J.; Longerich, S.; Mackfeld, U.; Jaeger, K. E.; Wiechert, W.; Pohl, M.; Krauss, U., Tailoring the properties of (catalytically)-active inclusion bodies. *Microbial cell factories* **2019,** *18* (1), 33.

6. (a) Talafova, K.; Hrabarova, E.; Chorvat, D.; Nahalka, J., Bacterial inclusion bodies as potential synthetic devices for pathogen recognition and a therapeutic substance release. *Microbial cell factories* **2013,** *12*, 16; (b) Vazquez, E.; Corchero, J. L.; Burgueno, J. F.; Seras-

Franzoso, J.; Kosoy, A.; Bosser, R.; Mendoza, R.; Martinez-Lainez, J. M.; Rinas, U.; Fernandez, E.; Ruiz-Avila, L.; Garcia-Fruitos, E.; Villaverde, A., Functional inclusion bodies produced in bacteria as naturally occurring nanopills for advanced cell therapies. *Advanced materials* **2012,** *24* (13), 1742-7; (c) Liovic, M.; Ozir, M.; Zavec, A. B.; Peternel, S.; Komel, R.; Zupancic, T., Inclusion bodies as potential vehicles for recombinant protein delivery into epithelial cells. *Microbial cell factories* **2012,** *11*, 67; (d) Stamm, A.; Strauss, S.; Vogt, P.; Scheper, T.; Pepelanova, I., Positive in vitro wound healing effects of functional inclusion bodies of a lipoxygenase from the Mexican axolotl. *Microbial cell factories* **2018,** *17* (1), 57; (e) Pesarrodona, M.; Jauset, T.; Díaz - Riascos, Z. V.; Sánchez - Chardi, A.; Beaulieu, M. E.; Seras - Franzoso, J.; Sánchez - García, L.; Baltà - Foix, R.; Mancilla, S.; Fernández, Y.; Rinas, U.; Schwartz, S.; Soucek, L.; Villaverde, A.; Abasolo, I.; Vázquez, E., Targeting Antitumoral Proteins to Breast Cancer by Local Administration of Functional Inclusion Bodies. *Advanced science* **2019,** *https://doi.org/10.1002/advs.201900849*.

7. Garcia-Fruitos, E.; Rodriguez-Carmona, E.; Diez-Gil, C.; Ferraz, R. M.; Vazquez, E.; Corchero, J. L.; Cano-Sarabia, M.; Ratera, I.; Ventosa, N.; Veciana, J.; Villaverde, A., Surface Cell Growth Engineering Assisted by a Novel Bacterial Nanomaterial. *Advanced materials* **2009,** *21* (42), 4249-+.

8. Seras-Franzoso, J.; Tatkiewicz, W. I.; Vazquez, E.; Garcia-Fruitos, E.; Ratera, I.; Veciana, J.; Villaverde, A., Integrating mechanical and biological control of cell proliferation through bioinspired multieffector materials. *Nanomedicine* **2015,** *10* (5), 873-91.

9. Unzueta, U.; Seras-Franzoso, J.; Cespedes, M. V.; Saccardo, P.; Cortes, F.; Rueda, F.; Garcia-Fruitos, E.; Ferrer-Miralles, N.; Mangues, R.; Vazquez, E.; Villaverde, A., Engineering tumor cell targeting in nanoscale amyloidal materials. *Nanotechnology* **2017,** *28* (1), 015102.

10. Cespedes, M. V.; Fernandez, Y.; Unzueta, U.; Mendoza, R.; Seras-Franzoso, J.; Sanchez-Chardi, A.; Alamo, P.; Toledo-Rubio, V.; Ferrer-Miralles, N.; Vazquez, E.; Schwartz, S.; Abasolo, I.; Corchero, J. L.; Mangues, R.; Villaverde, A., Bacterial mimetics of endocrine secretory granules as immobilized in vivo depots for functional protein drugs. *Scientific reports* **2016,** *6*, 35765.

11. Unzueta, U.; Cespedes, M. V.; Sala, R.; Alamo, P.; Sanchez-Chardi, A.; Pesarrodona, M.; Sanchez-Garcia, L.; Cano-Garrido, O.; Villaverde, A.; Vazquez, E.; Mangues, R.; Seras-Franzoso, J., Release of targeted protein nanoparticles from functional bacterial amyloids: A death star-like approach. *Journal of controlled release***2018**, *279*, 29.

12. Seras-Franzoso, J.; Sanchez-Chardi, A.; Garcia-Fruitos, E.; Vazquez, E.; Villaverde, A., Cellular uptake and intracellular fate of protein releasing bacterial amyloids in mammalian cells. *Soft matter* **2016,** *12* (14), 3451-60.

13. (a) Maji, S. K.; Perrin, M. H.; Sawaya, M. R.; Jessberger, S.; Vadodaria, K.; Rissman, R. A.; Singru, P. S.; Nilsson, K. P.; Simon, R.; Schubert, D.; Eisenberg, D.; Rivier, J.; Sawchenko, P.; Vale, W.; Riek, R., Functional amyloids as natural storage of peptide hormones in pituitary secretory granules. *Science* **2009,** *325* (5938), 328-32; (b) Jacob, R. S.; Das, S.; Ghosh, S.; Anoop, A.; Jha, N. N.; Khan, T.; Singru, P.; Kumar, A.; Maji, S. K., Amyloid formation of growth hormone in presence of zinc: Relevance to its storage in secretory granules. *Scientific reports* **2016,** *6*, 23370; (c) Wang, L.; Maji, S. K.; Sawaya, M. R.; Eisenberg, D.; Riek, R., Bacterial inclusion bodies contain amyloid-like structure. *PLoS biology* **2008,** *6* (8), e195.

14. (a) Tamamura, H.; Arakaki, R.; Funakoshi, H.; Imai, M.; Otaka, A.; Ibuka, T.; Nakashima, H.; Murakami, T.; Waki, M.; Matsumoto, A.; Yamamoto, N.; Fujii, N., Effective lowly cytotoxic analogs of an HIV-cell fusion inhibitor, T22 ([Tyr5,12, Lys7]-polyphemusin II). *Bioorganic & medicinal chemistry* **1998,** *6* (2), 231-8; (b) Tamamura, H.; Imai, M.; Ishihara, T.; Masuda, M.; Funakoshi, H.; Oyake, H.; Murakami, T.; Arakaki, R.; Nakashima,

H.; Otaka, A.; Ibuka, T.; Waki, M.; Matsumoto, A.; Yamamoto, N.; Fujii, N., Pharmacophore identification of a chemokine receptor (CXCR4) antagonist, T22 ([Tyr(5,12),Lys7]-polyphemusin II), which specifically blocks T cell-line-tropic HIV-1 infection. *Bioorganic & medicinal chemistry* **1998,** *6* (7), 1033-41.

15. Cespedes, M. V.; Unzueta, U.; Avino, A.; Gallardo, A.; Alamo, P.; Sala, R.; Sanchez-Chardi, A.; Casanova, I.; Mangues, M. A.; Lopez-Pousa, A.; Eritja, R.; Villaverde, A.; Vazquez, E.; Mangues, R., Selective depletion of metastatic stem cells as therapy for human colorectal cancer. *EMBO molecular medicine* **2018**. *10*, pii: e8772.

16. Pastan, I., Immunotoxins containing Pseudomonas exotoxin A: a short history. *Cancer immunology, immunotherapy : CII* **2003,** *52* (5), 338-41.

17. Sanchez-Garcia, L.; Serna, N.; Alamo, P.; Sala, R.; Cespedes, M. V.; Roldan, M.; Sanchez-Chardi, A.; Unzueta, U.; Casanova, I.; Mangues, R.; Vazquez, E.; Villaverde, A., Self-assembling toxin-based nanoparticles as self-delivered antitumoral drugs. *Journal of controlled release* **2018,** *274*, 81-92.

18. (a) Kim, H. Y.; Hwang, J. Y.; Kim, S. W.; Lee, H. J.; Yun, H. J.; Kim, S.; Jo, D. Y., The CXCR4 Antagonist AMD3100 Has Dual Effects on Survival and Proliferation of Myeloma Cells In Vitro. *Cancer research and treatment : official journal of Korean Cancer Association* **2010,** *42* (4), 225-34; (b) Kim, J.; Connelly, K. L.; Unterwald, E. M.; Rawls, S. M., Chemokines and cocaine: CXCR4 receptor antagonist AMD3100 attenuates cocaine place preference and locomotor stimulation in rats. *Brain, behavior, and immunity* **2016**; (c) Jung, Y. H.; Lee, D. Y.; Cha, W.; Kim, B. H.; Sung, M. W.; Kim, K. H.; Ahn, S. H., Antitumor effect of CXCR4 antagonist AMD3100 on the tumorigenic cell line of BHP10-3 papillary thyroid cancer cells. *Head & neck* **2016,** *38* (10), 1479-86.

19. Sanchez, J. M.; Sanchez-Garcia, L.; Pesarrodona, M.; Serna, N.; Sanchez-Chardi, A.; Unzueta, U.; Mangues, R.; Vazquez, E.; Villaverde, A., Conformational Conversion during

Controlled Oligomerization into Nonamylogenic Protein Nanoparticles. *Biomacromolecules* **2018,** *19* (9), 3788-3797.

20. Falgas, A.; Pallares, V.; Unzueta, U.; Cespedes, M. V.; Arroyo-Solera, I.; Moreno, M. J.; Gallardo, A.; Mangues, M. A.; Sierra, J.; Villaverde, A.; Vazquez, E.; Mangues, R.; Casanova, I., A CXCR4-targeted nanocarrier achieves highly selective tumor uptake in diffuse large B-cell lymphoma mouse models. *Haematologica* **2019**.

21. Li, J.; Mooney, D. J., Designing hydrogels for controlled drug delivery. *Nature reviews. Materials* **2016,** *1* (12).

22. (a) Vallet-Regi, M., Ordered mesoporous materials in the context of drug delivery systems and bone tissue engineering. *Chemistry* **2006,** *12* (23), 5934-43; (b) Koshy, S. T.; Zhang, D. K. Y.; Grolman, J. M.; Stafford, A. G.; Mooney, D. J., Injectable nanocomposite cryogels for versatile protein drug delivery. *Acta biomaterialia* **2018,** *65*, 36-43; (c) Lvov, Y. M.; DeVilliers, M. M.; Fakhrullin, R. F., The application of halloysite tubule nanoclay in drug delivery. *Expert opinion on drug delivery* **2016,** *13* (7), 977-86.

23. (a) Wu, Z.; Hao, N.; Zhang, H.; Guo, Z.; Liu, R.; He, B.; Li, S., Mesoporous iron-carboxylate metal-organic frameworks synthesized by the double-template method as a nanocarrier platform for intratumoral drug delivery. *Biomaterials science* **2017,** *5* (5), 1032-1040; (b) Chowdhury, M. A., Metal-organic-frameworks for biomedical applications in drug delivery, and as MRI contrast agents. *Journal of biomedical materials research. Part A* **2017,** *105* (4), 1184-1194; (c) Ibrahim, M.; Sabouni, R.; Husseini, G. A., Anti-cancer Drug Delivery Using Metal Organic Frameworks (MOFs). *Current medicinal chemistry* **2017,** *24* (2), 193-214; (d) Baeza, A.; Ruiz-Molina, D.; Vallet-Regi, M., Recent advances in porous nanoparticles for drug delivery in antitumoral applications: inorganic nanoparticles and nanoscale metal-organic frameworks. *Expert opinion on drug delivery* **2017,** *14* (6), 783-796; (e) Rojas, S.; Colinet, I.; Cunha, D.; Hidalgo, T.; Salles, F.; Serre, C.; Guillou, N.; Horcajada, P., Toward Understanding Drug Incorporation and Delivery from Biocompatible Metal-

Organic Frameworks in View of Cutaneous Administration. *ACS omega* **2018,** *3* (3), 2994-3003; (f) Dong, K.; Zhang, Y.; Zhang, L.; Wang, Z.; Ren, J.; Qu, X., Facile preparation of metal-organic frameworks-based hydrophobic anticancer drug delivery nanoplatform for targeted and enhanced cancer treatment. *Talanta* **2019,** *194*, 703-708; (g) Gandara-Loe, J.; Ortuno-Lizaran, I.; Fernandez-Sanchez, L.; Alio, J. L.; Cuenca, N.; Vega-Estrada, A.; Silvestre-Albero, J., Metal-Organic Frameworks as Drug Delivery Platforms for Ocular Therapeutics. *ACS applied materials & interfaces* **2019,** *11* (2), 1924-1931; (h) Gupta, V.; Tyagi, S.; Paul, A. K., Development of Biocompatible Iron-Carboxylate Metal Organic Frameworks for pH-Responsive Drug Delivery Application. *Journal of nanoscience and nanotechnology* **2019,** *19* (2), 646-654.

24. Rodriguez-Carmona, E.; Cano-Garrido, O.; Seras-Franzoso, J.; Villaverde, A.; Garcia-Fruitos, E., Isolation of cell-free bacterial inclusion bodies. *Microbial cell factories* **2010,** *9*, 71.

25. Rueda, F.; Cano-Garrido, O.; Mamat, U.; Wilke, K.; Seras-Franzoso, J.; Garcia-Fruitos, E.; Villaverde, A., Production of functional inclusion bodies in endotoxin-free Escherichia coli. *Applied microbiology and biotechnology* **2014,** *98* (22), 9229-38.

26. Cano-Garrido, O.; Sanchez-Chardi, A.; Pares, S.; Giro, I.; Tatkiewicz, W. I.; Ferrer-Miralles, N.; Ratera, I.; Natalello, A.; Cubarsi, R.; Veciana, J.; Bach, A.; Villaverde, A.; Aris, A.; Garcia-Fruitos, E., Functional protein-based nanomaterial produced in microorganisms recognized as safe: A new platform for biotechnology. *Acta biomaterialia* **2016,** *43*, 230-9.

27. Rueda, F.; Gasser, B.; Sanchez-Chardi, A.; Roldan, M.; Villegas, S.; Puxbaum, V.; Ferrer-Miralles, N.; Unzueta, U.; Vazquez, E.; Garcia-Fruitos, E.; Mattanovich, D.; Villaverde, A., Functional inclusion bodies produced in the yeast Pichia pastoris. *Microbial cell factories* **2016,** *15* (1), 166.

28. Corchero, J. L.; Gasser, B.; Resina, D.; Smith, W.; Parrilli, E.; Vazquez, F.; Abasolo, I.; Giuliani, M.; Jantti, J.; Ferrer, P.; Saloheimo, M.; Mattanovich, D.; Schwartz, S., Jr.;

Tutino, M. L.; Villaverde, A., Unconventional microbial systems for the cost-efficient production of high-quality protein therapeutics. *Biotechnology advances* **2013,** *31* (2), 140-53.

29. (a) Yun, Y. H.; Lee, B. K.; Park, K., Controlled Drug Delivery: Historical perspective for the next generation. *Journal of controlled release : official journal of the Controlled Release Society* **2015,** *219*, 2-7; (b) Turner, M. R.; Balu-Iyer, S. V., Challenges and Opportunities for the Subcutaneous Delivery of Therapeutic Proteins. *Journal of pharmaceutical sciences* **2018,** *107* (5), 1247-1260.

30. Serna, N.; Sanchez-Garcia, L.; Unzueta, U.; Diaz, R.; Vazquez, E.; Mangues, R.; Villaverde, A., Protein-Based Therapeutic Killing for Cancer Therapies. *Trends in biotechnology* **2018,** *36* (3), 318-335.

31. Song, J. S.; Kang, C. M.; Kang, H. H.; Yoon, H. K.; Kim, Y. K.; Kim, K. H.; Moon, H. S.; Park, S. H., Inhibitory effect of CXC chemokine receptor 4 antagonist AMD3100 on bleomycin induced murine pulmonary fibrosis. *Experimental & molecular medicine* **2010,** *42* (6), 465-72.

32. (a) Sausville, E. A.; Burger, A. M., Contributions of human tumor xenografts to anticancer drug development. *Cancer research* **2006,** *66* (7), 3351-4, discussion 3354; (b) Jin, K.; Teng, L.; Shen, Y.; He, K.; Xu, Z.; Li, G., Patient-derived human tumour tissue xenografts in immunodeficient mice: a systematic review. *Clin Transl Oncol* **2010,** *12* (7), 473-80.

33. (a) Lai, Y.; Wei, X.; Lin, S.; Qin, L.; Cheng, L.; Li, P., Current status and perspectives of patient-derived xenograft models in cancer research. *Journal of hematology & oncology* **2017,** *10* (1), 106; (b) Cassidy, J. W.; Caldas, C.; Bruna, A., Maintaining Tumor Heterogeneity in Patient-Derived Tumor Xenografts. *Cancer research* **2015,** *75* (15), 2963-8.

34. Cespedes, M. V.; Espina, C.; Garcia-Cabezas, M. A.; Trias, M.; Boluda, A.; Gomez del Pulgar, M. T.; Sancho, F. J.; Nistal, M.; Lacal, J. C.; Mangues, R., Orthotopic microinjection of human colon cancer cells in nude mice induces tumor foci in all clinically relevant metastatic sites. *The American journal of pathology* **2007,** *170* (3), 1077-85.

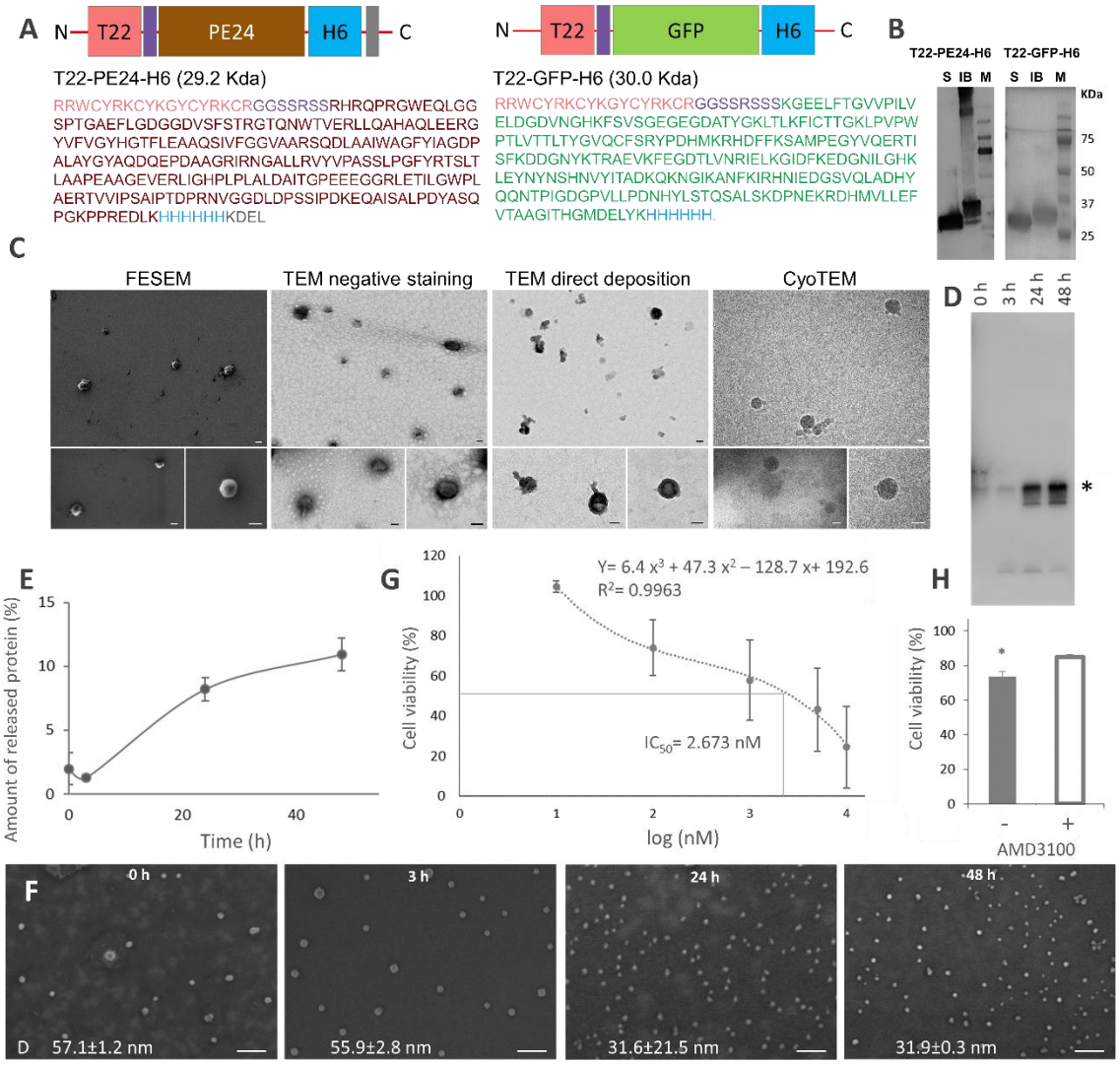

Figure 1. Structural and functional characterization of PE24-based IBs. A. Scheme of the modular protein and amino acid sequence of T22-PE24-H6 (left) and of the irrelevant, closely related modular protein T22-GFP-H6 (right). B. Immunodetection of T22-PE24-H6 and T22-GFP-H6 in form of purified soluble protein (S) and IBs, by anti-His WB. M is the molecular marker. C. Representative FESEM, TEM (direct deposition and negative staining) and cryoTEM images of PE24-based IBs. Size bars represent 200 nm. D. Protein release from T22-PE24-H6 IBs at different times (0, 3, 24 and 48 h) determined by WB with 1/4000 anti-His (Genescript ref. A00186-100). The asterisk shows the full T22-PE24-H6. E. Relative

protein amount of in vitro protein release from T22-PE24-H6 IBs at different times (0, 3, 24 and 48 h) determined by WB with 1/4000 anti-His (Genescript ref. A00186-100) by triplicate. F. Representative FESEM images and quantification of T22-PE24-H6 nanoparticles released from IBs at different times (0, 3, 24, and 48 h). Size bars represent 200 nm Quantitative data were expressed as $\bar{x} \pm SD$. Relevant statistical differences were expressed as * $p < 0.05$. D is the mean nanoparticle diameter measured over the FESEM images.in each sample. G. Viability of cultured HeLa cells exposed to different PE24-based IBs concentrations (10, 100, 1000, 5000 and 10000 nM). Data was fit to a cubit equation, IC_{50} dose is 2676 nM H. AMD3100-mediated inhibition of cell mortality of cells exposed to T22-PE24-H6 IBs. Quantitative data were expressed as $\bar{x} \pm SD$. Relevant statistical differences were expressed as * $p < 0.05$.

.

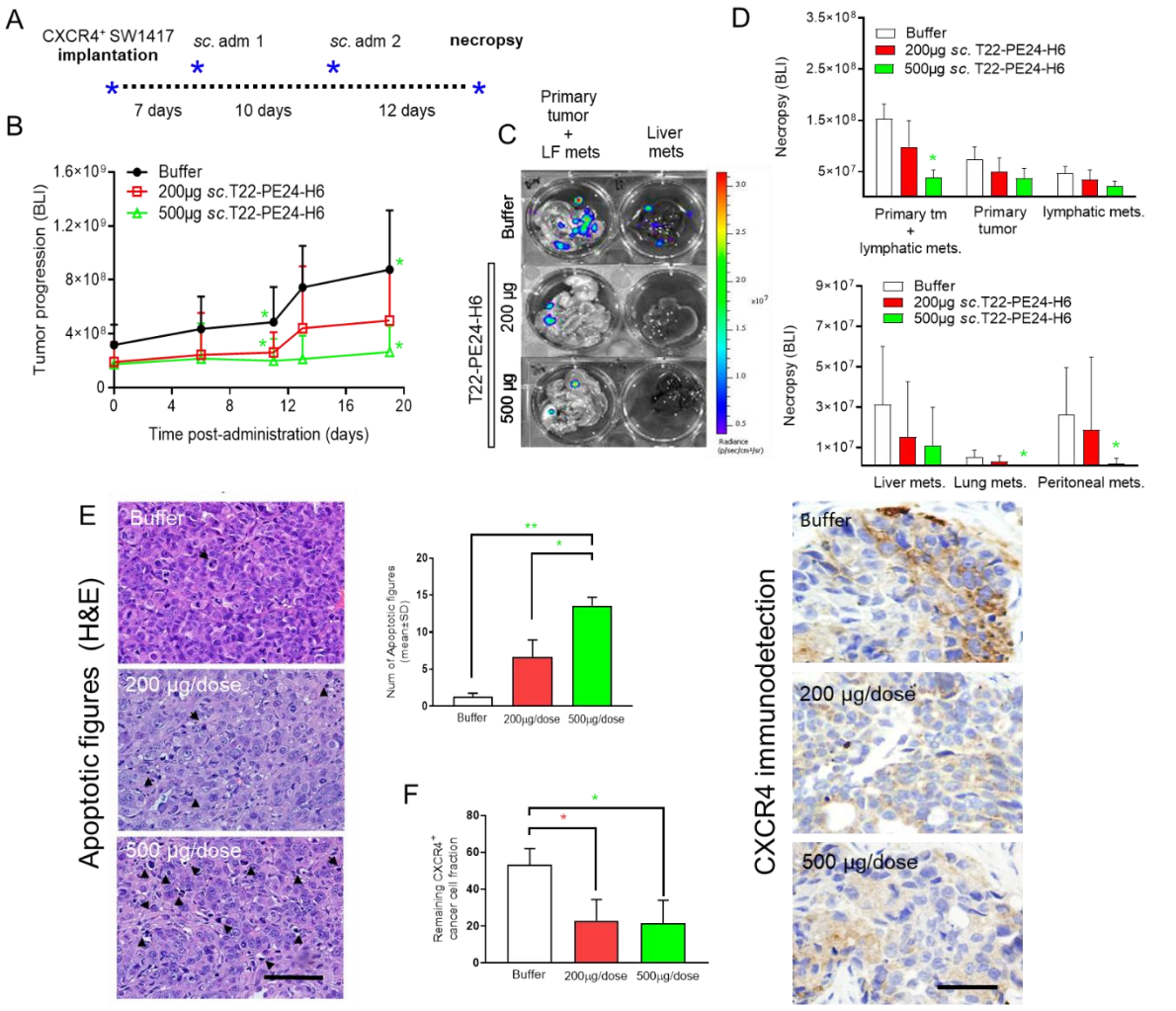

Figure 2. Antineoplastic effect after subcutaneous administration of T22-PE24-H6 inclusion bodies. A. Design and administration regime used in the *in vivo* experiment using the CXCR4$^+$ SW1417-derived orthotopic cancer model. A dose of 500 µg or 200 µg was given every 10 days period, and two doses total. B. Primary tumor and metastatic growth inhibition (C and D) at the different sites as measured by reduction of bioluminescence emission by SW1417-luciferase expressing cancer cells. Statistical significances: in tumor progression $*p = 0.042$ and $*p = 0.047$ between groups at day 13 and 19, respectively; $*p = 0.035$ in primary tumor + lymphatic metastases at necropsy; $*p = 0.046$ and $*p = 0.039$ in lung and peritoneal metastasis groups versus buffer group, respectively. E. Representative images and quantitation of apoptotic figures (white arrows) in primary tumor, detected by nuclear condensation or nuclear fragmentation after Hematoxylin-eosin staining at the end of

the experiment (n=5 mice/group; 10 fields/mouse as described in material and methods) * p =0.040 or ** p =0.009 F. Representative images and quantitations of the reduction of $CXCR4^+$ cell fraction in primary tumor assayed by CXCR4 immunodetection at the end of the experiment (n=5 mice/group).* p =0.037 and * p =0.038 comparisons between the control group and 200 and 500 µg/doses, respectively. Size bars represent 100 µm. Quantitative data were expressed as $\bar{x} \pm SD$.

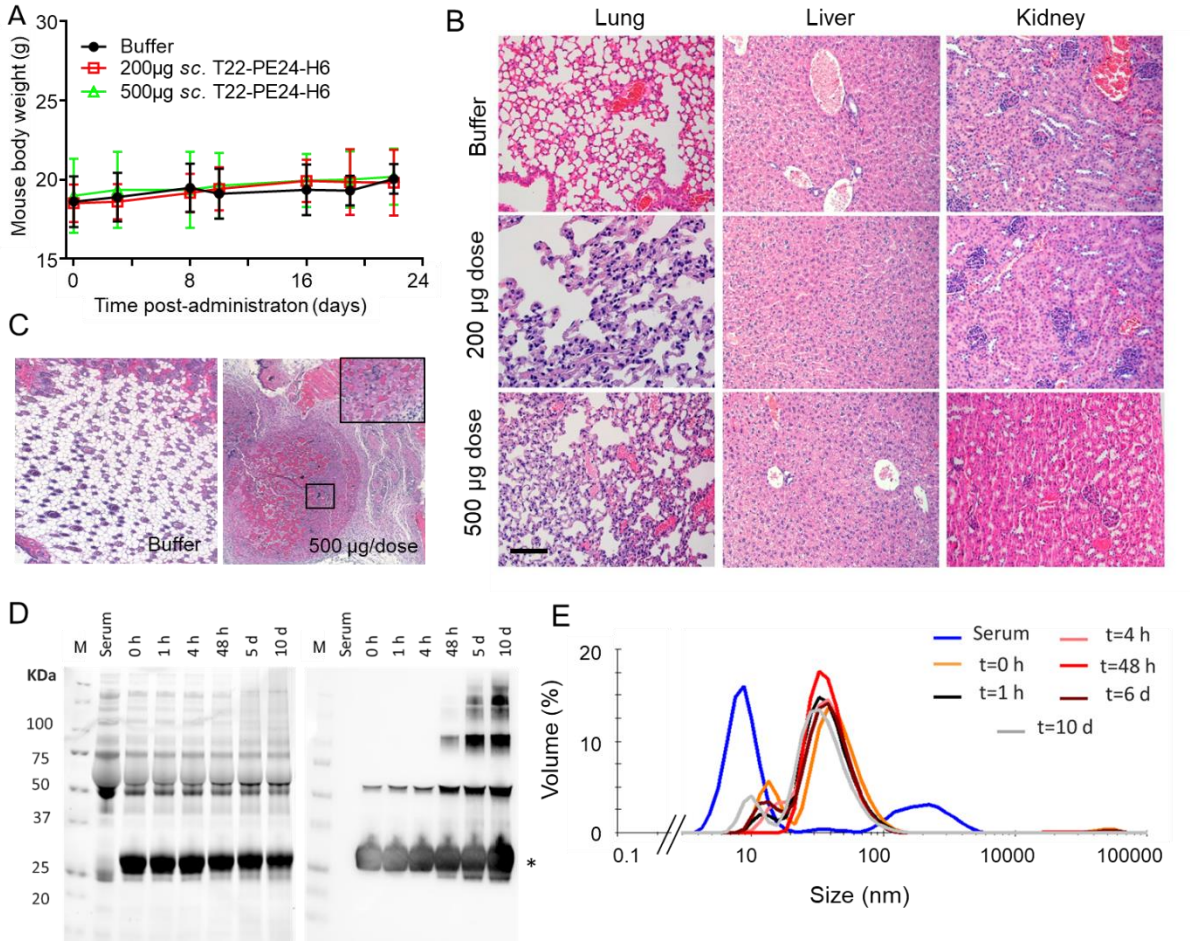

Figure 3. Lack of toxicity on major organs in T22-PE24-H6 treated mice. A. Lack of differences in mouse body weight among tested groups was registered along time in the SW1417-derived CCR model (Mean ± SEM, n=5 mice/group) B. Representative images showing lack of histopathological alterations in H&E-stained lung, liver and kidney at the end of the experiment after the SC administration of a 500 µg dose of T22-PE24-H6. Size bars represent 100 µm. C. Histological analysis on skin H&E stained samples in the injection point showing no oedema, material deposition or massive inflammatory cell infiltration, except for the presence of lymphocytes (see insert) at the highest 500 µg dose. D. Protein integrity during 10 days (d) of incubation in human serum a 37 ºC determined by full protein band detection (left) and by anti-His WB (right). The * indicates the expected position of the full-

length T22-PE24-H6. M is the molecular marker. E. Hydrodynamic size of the protein as determined by DLS, upon incubation with sera for different times.

Table 1. Reduction of metastatic foci induced by PE24 IBs treatment

Groups	Primary tumor	Lymphatic mets		Hepatic mets		Pulmonary mets		Peritoneal mets	
		*Mice rate ------- foci #	Area ($\bar{x} \pm SD$; μm^2)	*Mice rate ------- foci #	Area ($\bar{x} \pm SD$; μm^2)	*Mice Rate ------- foci #	Area ($\bar{x} \pm SD$; μm^2)	*Mice Rate ------- foci #	Area ($\bar{x} \pm SD$; μm^2)
Buffer	5/5	5/5 93[a, b]	101267 ± 105531[g,h]	1/5 4	26954 ± 7385	3/5 27[c, d]	9299 ± 6839[i]	4/5 109[e, f]	350612 ± 301879[k]
200 µg/ dose	5/5	2/5 18[a]	18433 ± 19219[g]	0/5 0	0	1/5 5[c]	11252 ± 4950[j]	2/5 11[e]	237312 ± 505731
500 µg/ dose	5/5	2/5 13[b]	32616 ± 23944[h]	0/5 0	0	1/5 2[d]	3510 ± 2974[i, j]	2/5 10[f]	8722 ± 13149[k]

Significant differences at [a]p= 0.030; [b]p= 0.021; [c]p= 0.024; [d]p= 0.012; [e]p< 0.0001; [f]p< 0.0001; [g]p= 0.041; [h]p= 0.045; [i]p= 0.043; [j]p= 0.038; [k]p= 0.010. Fisher's exact test used to detect differences between control and experimental groups of affected mice regarding metastatic rates at the different organs. Non-parametric multiple comparisons were applied to compare the number and size of metastatic foci in the affected organs (see M&M). Abbreviation: *Mice rate, mice with tumor foci at the indicated site/total number of mice per group; foci#, number of foci in this particular site and group.

Bacterial inclusion bodies have been engineered as secretory amyloids for subcutaneous implantation and physiological release of antitumoral protein drugs. These granules slowly secrete self-assembling, CXCR4-targeted protein nanoparticles based on the *Pseudomonas* exotoxin that selectively destroy metastatic colorectal cancer stem cells, promoting a dramatic reduction of metastatic foci in absence of undesired side toxicity.

Keyword protein materials, secretory amyloids, self-assembling, drug release, metastatic cancer

María Virtudes Céspedes, Olivia Cano-Garrido, Patricia Álamo, Rita Sala, Alberto Gallardo, Naroa Serna, Eric Voltà-Durán, Alejandro Sánchez- Chardi, Hèctor López-Laguna, Laura Sánchez-García, Julieta M. Sánchez, Ugutz Unzueta, Esther Vázquez, Ramón Mangues*, Antonio Villaverde**

Engineering secretory amyloids for remote and highly selective destruction of metastatic foci

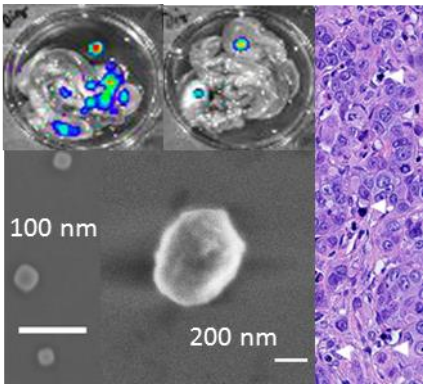

Supporting Information

Engineering secretory amyloids for remote and highly selective destruction of metastatic foci

María Virtudes Céspedes, Olivia Cano-Garrido, Patricia Álamo, Rita Sala, Alberto Gallardo, Naroa Serna, Eric Voltà-Durán, Alejandro Sánchez-Chardi, Hèctor López-Laguna, *Laura Sánchez-García, Julieta M. Sánchez, Ugutz Unzueta, Esther Vázquez, Ramón Mangues, Antonio Villaverde*

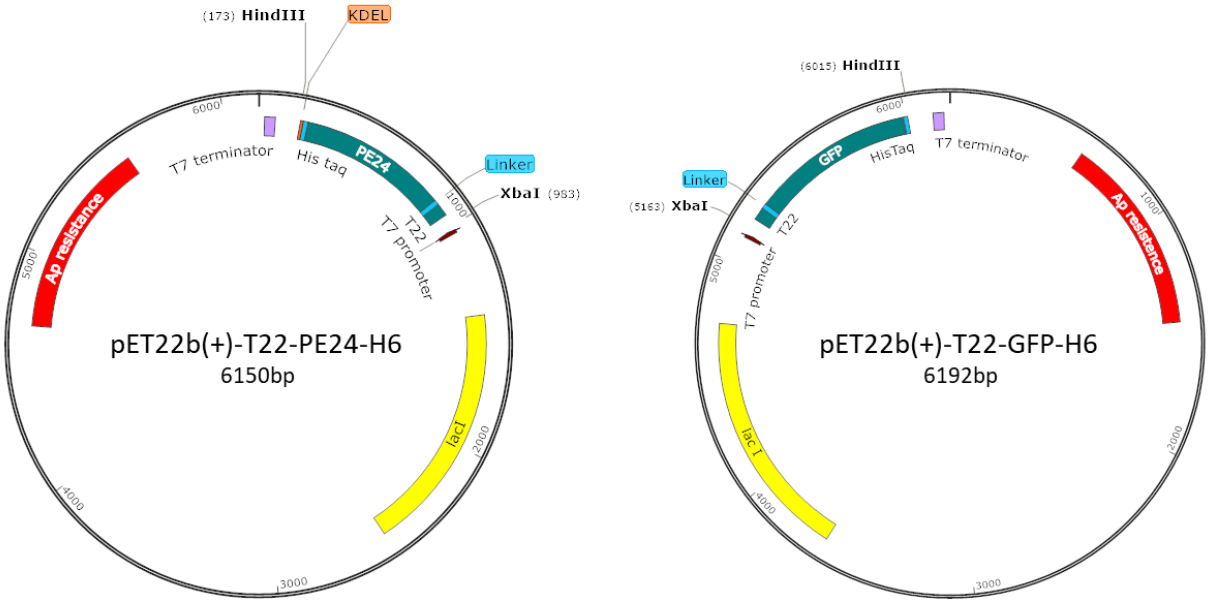

Figure S1: Maps of protein-encoding plasmids for the biological production of T22-PE24-H6 (left) and T22-GFP-H6 (right).

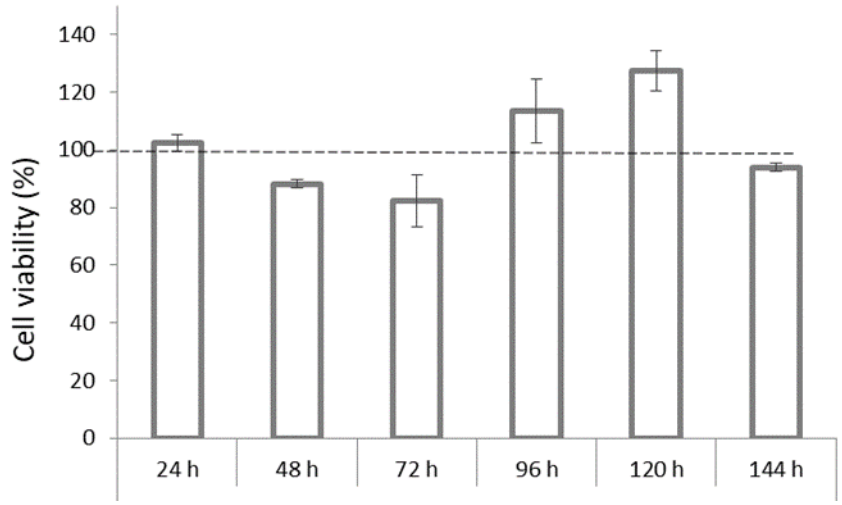

Figure S2: Viability of cultured HeLa cells exposed to 1 µM of T22-GFP-H6 IBs at different incubation times (24, 48, 72, 96, 120 and 144 h) compared untreated cells (dashed line). The standard deviation is represented by grey lines at each sample. Differences between bars are not significant and the observed slight fluctuation of data is due to the necessary addition of fresh media at day 4 to keep cell viability throughout the experiment.

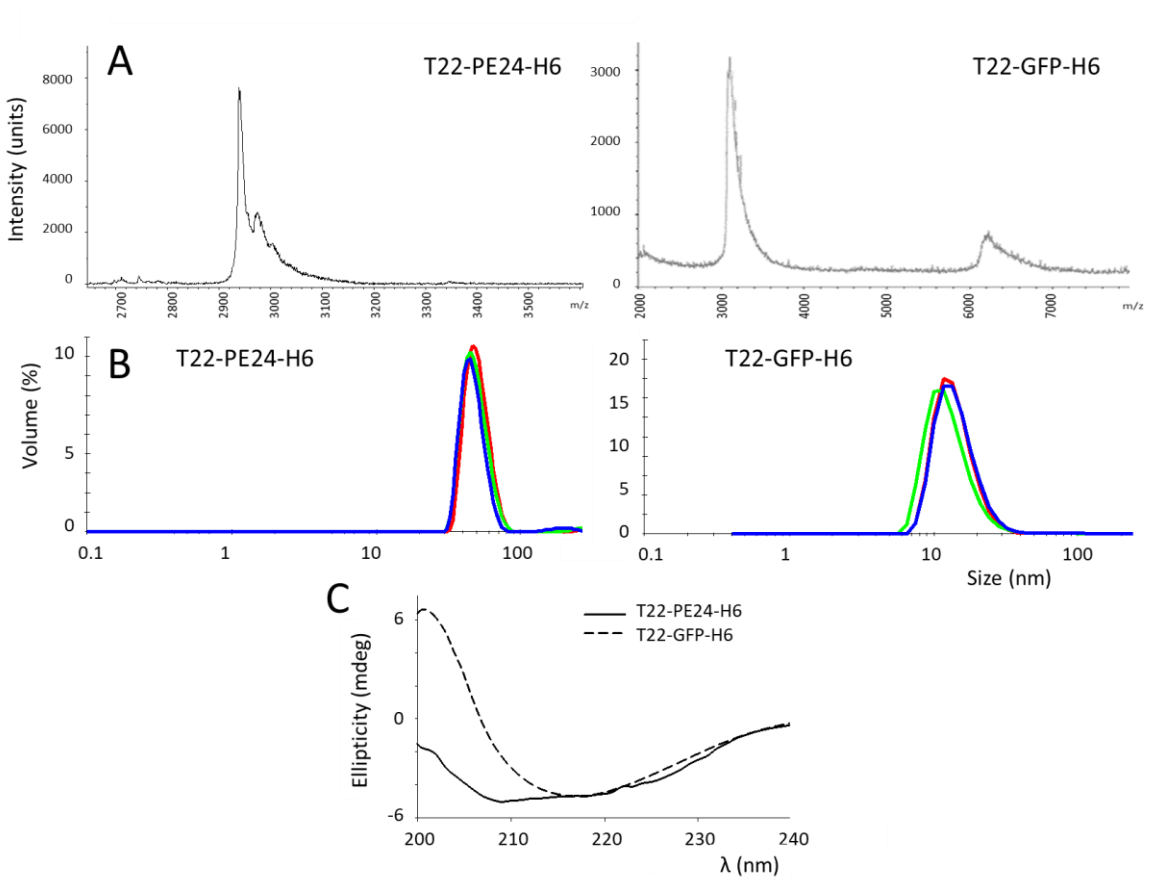

Figure S3: Physicochemical characterization of the modular proteins. A. Mass spectroscopy of pure T22-PE24-H6 (Peak: 29386.69 Da) and T22-GFP-H6 (Peak: 31012.59 Da). B. Hydrodynamic size of T22-PE24-H6 and T22-GFP-H6 determined by DLS. Different lines indicate replicas. C. Far UV CD of T22-PE24-H6 and T22-GFP-H6 in carbonate-bicarbonate buffer at pH 8 measured at 25ºC.

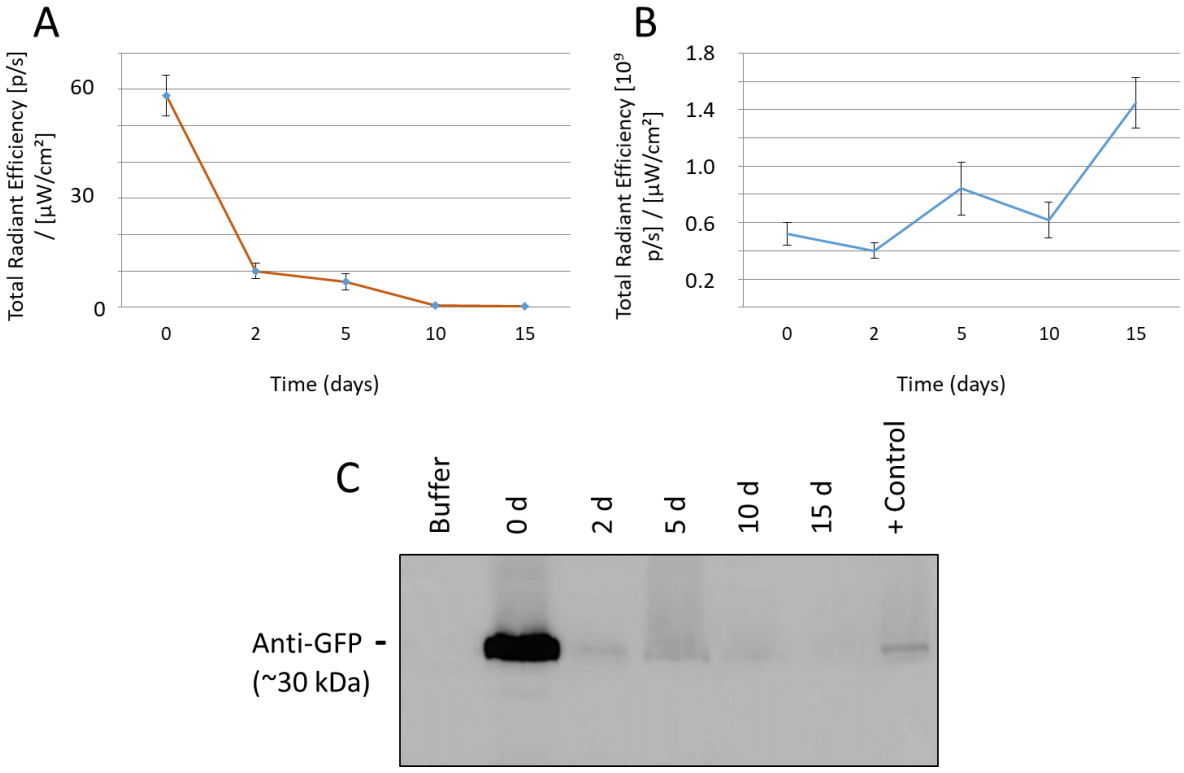

Figure S4. Kinetics of disaggregation of T22-GFP-H6 IBs at the injection site and nanoparticle uptake in tumor tissue, upon 1 mg single SC T22-GFP-H6 IBs dose. A. Reduction in total fluorescence emission (FLI) at the injection site after subcutaneous injection of 1 mg of T22-GFP-H6 IBs in $CXCR4^{+}$ tumor bearing mice (n=3 per point) along time. B. Sustained increase of total fluorescence emission (FLI) in tumor tissue of mice (n=3 per point) after injection of IBs at a remote site along time (0, 2, 5, 10 and 15 days). FLI was measured using the IVIS Spectrum equipment. C. Kinetics of protein reduction at the injection site, measured by WB using an anti-GFP mAb along the 0-15 days (d) period, after 1 mg SC injection of T22-GFP-H6 IBs. Positive Control: Toledo cell line with internalized soluble T22-GFP-H6 nanoparticles.

Table S1. Lack of antitumor and antimetastatic effect of T22-GFP-H6 IBs in a colorectal cancer model *

	Primary tumor Total Flux [p/s]	Metastatic dissemination							
		Lymphatic		Liver		Lung		Peritoneal	
		Foci (n)	Area (mean± SD, μm^2)	Foci (n)	Area (mean± SD, μm^2)	Foci (n)	Area (mean± SD, μm^2)	Foci (n)	Area (mean± SD, μm^2)
Buffer	1.41E+08 [a]	81	56283 ±111849	53	9777±11066	13	4674±6599	33	28323±60145
T22-GFP-H6 IBs	2.56E+08[a]	69	19546± 42215	40	12882±12958	35	7823±7582	29	134555±276032

* T22-GFP-H6 IBs were administered SC at 500 μg dose x 2 doses at a10-day interval. n=6 mice per group.

** Luminescence emitted by the primary tumor at the end of the experiment as measured using the IVIS Spectrum equipment.

*** Number of metastatic foci counted in 6 not consecutive H&E stained sections of tissues at the organs where colorectal cancer disseminates.

[a]p=0.064 (Student t test).